5D-Tracking of a nanorod in a focused laser beam - a theoretical concept

Markus Grießhammer and Alexander Rohrbach*

Laboratory for Bio- and Nano- Photonics, Department of Microsystems Engineering-IMTEK, University of Freiburg, Georges Köhler Allee 102,79110 Freiburg, Germany

**rohrbach@imtek.de*

Abstract: Back-focal plane (BFP) interferometry is a very fast and precise method to track the 3D position of a sphere within a focused laser beam using a simple quadrant photo diode (QPD). Here we present a concept of how to track and recover the 5D state of a cylindrical nanorod (3D position and 2 tilt angles) in a laser focus by analyzing the interference of unscattered light and light scattered at the cylinder. The analytical theoretical approach is based on Rayleigh-Gans scattering together with a local field approximation for an infinitely thin cylinder. The approximated BFP intensities compare well with those from a more rigorous numerical approach. It turns out that a displacement of the cylinder results in a modulation of the BFP intensity pattern, whereas a tilt of the cylinder results in a shift of this pattern. We therefore propose the concept of a local QPD in the BFP of a detection lens, where the QPD center is shifted by the angular coordinates of the cylinder tilt.

OCIS codes: (120.0120) Instrumentation, measurement, and metrology; (140.7010) Laser trapping; (260.3160) Interference; (290.0290) Scattering; (070.0070) Fourier optics and signal processing.

References and links

1. A. P. Bartko and R. M. Dickson, "Imaging three-dimensional single molecule orientations," J. Phys. Chem. B **103**(51), 11237–11241 (1999).
2. K. I. Mortensen, L. S. Churchman, J. A. Spudich, and H. Flyvbjerg, "Optimized localization analysis for single-molecule tracking and super-resolution microscopy," Nat. Methods **7**(5), 377–381 (2010).
3. S. Stallinga and B. Rieger, "Position and orientation estimation of fixed dipole emitters using an effective Hermite point spread function model," Opt. Express **20**(6), 5896–5921 (2012).
4. M. Böhmer and J. Enderlein, "Orientation imaging of single molecules by wide-field epifluorescence microscopy," J. Opt. Soc. Am. B **20**(3), 554–559 (2003).
5. P. J. Pauzauskie, A. Radenovic, E. Trepagnier, H. Shroff, P. D. Yang, and J. Liphardt, "Optical trapping and integration of semiconductor nanowire assemblies in water," Nat. Mater. **5**(2), 97–101 (2006).
6. M. E. J. Friese, T. A. Nieminen, N. R. Heckenberg, and H. Rubinsztein-Dunlop, "Optical alignment and spinning of laser-trapped microscopic particles," Nature **394**(6691), 348–350 (1998).
7. E. L. Florin, J. K. H. Horber, and E. H. K. Stelzer, "High-resolution axial and lateral position sensing using two-photon excitation of fluorophores by a continuous-wave Nd alpha YAG laser," Appl. Phys. Lett. **69**(4), 446–448 (1996).
8. P. C. Seitz, E. H. K. Stelzer, and A. Rohrbach, "Interferometric tracking of optically trapped probes behind structured surfaces: a phase correction method," Appl. Opt. **45**(28), 7309–7315 (2006).
9. Y. Nakayama, P. J. Pauzauskie, A. Radenovic, R. M. Onorato, R. J. Saykally, J. Liphardt, and P. Yang, "Tunable nanowire nonlinear optical probe," Nature **447**(7148), 1098–1101 (2007).
10. D. B. Phillips, J. A. Grieve, S. N. Olof, S. J. Kocher, R. Bowman, M. J. Padgett, M. J. Miles, and D. M. Carberry, "Surface imaging using holographic optical tweezers," Nanotechnology **22**(28), 285503 (2011).
11. A. A. M. Bui, A. B. Stilgoe, T. A. Nieminen, and H. Rubinsztein-Dunlop, "Calibration of nonspherical particles in optical tweezers using only position measurement," Opt. Lett. **38**(8), 1244–1246 (2013).
12. S. J. Parkin, G. Knöner, T. A. Nieminen, N. R. Heckenberg, and H. Rubinsztein-Dunlop, "Picoliter viscometry using optically rotated particles," Phys. Rev. E Stat. Nonlin. Soft Matter Phys. **76**(4), 041507 (2007).
13. D. G. Grier, "A revolution in optical manipulation," Nature **424**(6950), 810–816 (2003).
14. M. Speidel, L. Friedrich, and A. Rohrbach, "Interferometric 3D tracking of several particles in a scanning laser focus," Opt. Express **17**(2), 1003–1015 (2009).

15. D. Ruh, B. Tränkle, and A. Rohrbach, "Fast parallel interferometric 3D tracking of numerous optically trapped particles and their hydrodynamic interaction," Opt. Express **19**(22), 21627–21642 (2011).
16. K. Dholakia and T. Cizmar, "Shaping the future of manipulation," Nat. Photonics **5**(6), 335–342 (2011).
17. S. H. Simpson and S. Hanna, "Optical trapping of spheroidal particles in Gaussian beams," J. Opt. Soc. Am. A **24**(2), 430–443 (2007).
18. F. Borghese, P. Denti, R. Saija, M. A. Iati, and O. M. Marago, "Radiation torque and force on optically trapped linear nanostructures," Phys. Rev. Lett. **100**, 163903 (2008).
19. P. B. Bareil and Y. Sheng, "Angular and position stability of a nanorod trapped in an optical tweezers," Opt. Express **18**(25), 26388–26398 (2010).
20. S. H. Simpson and S. Hanna, "First-order nonconservative motion of optically trapped nonspherical particles," Phys. Rev. E Stat. Nonlin. Soft Matter Phys. **82**(3), 031141 (2010).
21. Y. Cao, A. B. Stilgoe, L. Chen, T. A. Nieminen, and H. Rubinsztein-Dunlop, "Equilibrium orientations and positions of non-spherical particles in optical traps," Opt. Express **20**(12), 12987–12996 (2012).
22. A. Irrera, P. Artoni, R. Saija, P. G. Gucciardi, M. A. Iatì, F. Borghese, P. Denti, F. Iacona, F. Priolo, and O. M. Maragò, "Size-scaling in optical trapping of silicon nanowires," Nano Lett. **11**(11), 4879–4884 (2011).
23. P. J. Reece, W. J. Toe, F. Wang, S. Paiman, Q. Gao, H. H. Tan, and C. Jagadish, "Characterization of semiconductor nanowires using optical tweezers," Nano Lett. **11**(6), 2375–2381 (2011).
24. O. M. Maragò, P. H. Jones, F. Bonaccorso, V. Scardaci, P. G. Gucciardi, A. G. Rozhin, and A. C. Ferrari, "Femtonewton force sensing with optically trapped nanotubes," Nano Lett. **8**(10), 3211–3216 (2008).
25. L. Dixon, F. C. Cheong, and D. G. Grier, "Holographic deconvolution microscopy for high-resolution particle tracking," Opt. Express **19**(17), 16410–16417 (2011).
26. A. Pralle, M. Prummer, E. L. Florin, E. H. K. Stelzer, and J. K. H. Hörber, "Three-dimensional high-resolution particle tracking for optical tweezers by forward scattered light," Microsc. Res. Tech. **44**(5), 378–386 (1999).
27. A. Rohrbach, C. Tischer, D. Neumayer, E. L. Florin, and E. H. K. Stelzer, "Trapping and tracking a local probe with a photonic force microscope," Rev. Sci. Instrum. **75**(6), 2197–2210 (2004).
28. G. Volpe, G. Kozyreff, and D. Petrov, "Backscattering position detection for photonic force microscopy," J. Appl. Phys. **102**(8), 084701 (2007).
29. R. Huang, I. Chavez, K. M. Taute, B. Lukic, S. Jeney, M. G. Raizen, and E.-L. Florin, "Direct observation of the full transition from ballistic to diffusive Brownian motion in a liquid," Nat. Phys. **7**(7), 576–580 (2011).
30. L. Friedrich and A. Rohrbach, "Improved interferometric tracking of trapped particles using two frequency-detuned beams," Opt. Lett. **35**(11), 1920–1922 (2010).
31. H. Kress, E. H. K. Stelzer, and A. Rohrbach, "Tilt angle dependent three-dimensional-position detection of a trapped cylindrical particle in a focused laser beam," Appl. Phys. Lett. **84**(21), 4271–4273 (2004).
32. L. Friedrich and A. Rohrbach, "Tuning the detection sensitivity: a model for axial backfocal plane interferometric tracking," Opt. Lett. **37**(11), 2109–2111 (2012).
33. A. Rohrbach and E. H. K. Stelzer, "Optical trapping of dielectric particles in arbitrary fields," J. Opt. Soc. Am. A **18**(4), 839–853 (2001).
34. M. M. Tirado, C. L. Martinez, and J. G. Delatorre, "Comparison of theories for the translational and rotational diffusion coefficients of rod-like macromolecules. Applications to short DNA fragments," J. Chem. Phys. **81**(4), 2047–2052 (1984).
35. A. Rohrbach, H. Kress, and E. H. K. Stelzer, "Three-dimensional tracking of small spheres in focused laser beams: influence of the detection angular aperture," Opt. Lett. **28**(6), 411–413 (2003).
36. M. Pelton, M. Z. Liu, H. Y. Kim, G. Smith, P. Guyot-Sionnest, and N. F. Scherer, "Optical trapping and alignment of single gold nanorods by using plasmon resonances," Opt. Lett. **31**(13), 2075–2077 (2006).
37. C. Selhuber-Unkel, I. Zins, O. Schubert, C. Sönnichsen, and L. B. Oddershede, "Quantitative optical trapping of single gold nanorods," Nano Lett. **8**(9), 2998–3003 (2008).

1. Introduction

In recent years optical tracking of nanorods and dipole emitters have attracted considerable interest in various disciplines. On the one hand, position and orientation tracking of dipolar light emitters such as fluorophores have led to a significant progress in localization microscopy techniques (e.g. STORM, PALM) enabling super-resolution optical imaging in three dimensions [1–3] or in biophysical single-molecule experiments [4]. On the other hand, nano-sized cylindrical rods can serve as flexible building-blocks in nano-technology because of various optical and electrical properties, which can be controlled by their bulk material, size and environment [5]. Furthermore, nanorods point-out a strong potential as probes for photonic force microscopy to measure local hydrodynamics, to scan surfaces [6–11] or to determine visco-elastic environments [12], especially in bio-sciences.

The most promising tool to manipulate these nanorods in five dimensions (3 directions in displacement, 2 different orientations) are optical tweezers, which can easily be moved in 3D

space, can be multiplexed in space and time [13–15] or can be reshaped by computer-holograms [16].

Nanorods are advantageous for optical trapping because of their typically upright orientation due to an increased volume overlap with the axially extended laser focus. This leads to an increased overall polarizability and increased optical forces relative to spherical probes of comparable volumes [17–21]. The ability to measure changes in displacement and orientation either due to Brownian motion or due to external forces and torques make optically trapped nanorods a multi-modal and very sensitive sensor for the bio-nano-sciences [22]. This has been achieved recently with video microscopy, but the slow frame acquisition rates often make it impossible to measure microsecond position changes and millisecond relaxation times as relevant for many applications. Optical trapped nanorods have been tracked in their 2D position with quadrant photo diodes (QPD) [23] or with additional separation of the 3D position and 2D orientation fluctuation relaxations [24].

However, the simultaneous tracking of the 3D position and of the orientation of a nanorod without post-processing of camera images has not been achieved yet – neither with coherent nor with incoherent imaging [25].

The fastest and most precise 3D tracking technique is back focal plane (BFP) interferometry [26–28]. Although the tracking range is limited to the extents of a laser focus, tracking rates of more than 1MHz [29] can be achieved and precisions of 1-5 nm [27].

In this study we demonstrate theoretically how to achieve 5D tracking of a cylindrical probe in a highly focused laser beam by using back-focal plane interferometry. We show both numerically and analytically that the 3D position and 2D orientation of the nanorod can be determined over a sufficiently large range of displacements and orientations approximately independent of the other dimension. Due to a simple mapping scheme, hardly any post-processing is required enabling online-monitoring of the particle fluctuations.

2. Back focal plane interferometric tracking

The concept of back focal plane (BFP) interferometry to track the 3D position of a sphere is extended to track the 5D state of a cylindrical particle in a focused laser beam. This method exploits the interference of the light scattered at the particle and the unscattered light, which is captured by a detection lens DL (see Fig. 1). A sensor in the BFP records the interference intensity from the scattered and unscattered electric field.

2.1 Spherical particles

The intensity distribution $\tilde{I}(k_x, k_y, \mathbf{b})$, described by the Fourier plane coordinates k_x and k_y, changes uniquely with the position $\mathbf{b}(t) = (b_x(t), b_y(t), b_z(t))$ of the particle roughly over the extent of the laser focus.

The intensity distribution $\tilde{I}(k_x, k_y, \mathbf{b})$ in the BFP is a superposition of the incident $\tilde{E}_i(k_x, k_y)$ and the scattered field $\tilde{E}_s(k_x, k_y, \mathbf{b})$.

$$\begin{pmatrix} S_x \\ S_y \\ S_z \\ S_\theta \\ S_\phi \end{pmatrix} \approx \begin{pmatrix} S_{0x} \\ S_{0y} \\ S_{0z} \\ S_{0\theta} \\ S_{0\phi} \end{pmatrix} + \begin{pmatrix} g_{xx} & & & & \\ & g_{yy} & & & \\ & & g_{zz} & & \\ & & & g_{\theta\theta} & \\ & & & & g_{\phi\phi} \end{pmatrix} \begin{pmatrix} b_x \\ b_y \\ b_z \\ b_\theta \\ b_\phi \end{pmatrix} \qquad (1)$$

where the position dependent difference of the phase of the incident and scattered field can be separated for small displacements **b** into 3 nearly orthogonal phases $\Delta\Phi_j(b_j)$, which only depend on sphere displacements in direction b_j (with $j = x, y, z$):

$$\Delta\Phi\left(k_x,k_y,\mathbf{b}\right)=\Delta\Phi_x\left(k_x,k_y,b_x\right)+\Delta\Phi_y\left(\mathrm{k_x},\mathrm{k_y},\mathrm{b_y}\right)+\Delta\Phi_z\left(k_x,k_y,b_z\right) \qquad (2)$$

A small displacement b_j is a shift of not more than about half the FWHM extent of the focus in the specific direction $j = x, y, z$.

Typically two quadrant photo diodes (QPD) are used [30] for the 3D tracking of a spherical particle. QPD #1 is completely illuminated by $\tilde{I}\left(k_x,k_y,\mathbf{b}\right)$ and provides the lateral position signals $S_x(\mathbf{b})$ and $S_y(\mathbf{b})$, whereas QPD #2 only records the central part of $\tilde{I}(k_x,k_y,\mathbf{b})$ and provides the axial signals $S_z(\mathbf{b})$.

The three position signals $S_j(\mathbf{b})$, are extracted by integrating the intensity over a certain area, which is determined by a filter function $H_j(k_x, k_y)$.

$$S_j\left(\mathbf{b}\right)=\iint\tilde{I}\left(k_x,k_y,\mathbf{b}\right)H_j\left(k_x,k_y\right)dk_xdk_y \qquad (3)$$

The filter $H_x(k_x, k_y)$ generates the difference from the signals of the upper two and the lower two QPD-quadrants, whereas $H_y(k_x, k_y)$ generates the difference from the signals of the left and right quadrants. $H_z(k_x, k_y)$ simply generates the sum of all four quadrants to provide the axial position signal S_z.

For small displacements we assume the position signals to be linear and mutual orthogonal

$$S_j(b_j)=S_{0j}+\iint 2\sqrt{I_iI_s(b_j)}\,\cos\left(\Delta\Phi(b_j)\right)H_j\;dk_xdk_y\approx S_{0j}+g_jb_j \qquad (4)$$

The calibration factor g_j is the detector sensitivity in the direction $j = x, y, z$. The intensity offset S_{0j} is typically zero for the lateral directions and can be subtracted in z-direction.

Orthogonality means that a position signal for the displacement in one direction is independent of the displacement in all other directions such that $S_j(b_j)\;S_k(b_k) = \delta_{jk}$. The off-diagonal entries of the sensitivity matrix $\hat{\mathbf{g}}$ are negligibly small for small particle displacements:

$$\mathbf{S}\left(\mathbf{b}\right)\approx\mathbf{S}_0+\hat{\mathbf{g}}\cdot\mathbf{b} \qquad (5)$$

2.2 Cylindrical particles

For non-spherical particles, such as cylinders or ellipsoids, also their orientation is of interest. This requires two further orientation signals, which are more complicated to extract from the interference pattern $|\tilde{E}_i(k_x,k_y)+\tilde{E}_s(k_x,k_y,\mathbf{b})|^2$ since the phase changes due to particle re-orientations and particle displacements are coupled. For a cylinder tilted on its long axis, for example, the position signals lose then their property to be linear and orthogonal [31].

As indicated in Fig. 1, totally five signals $S_x(\mathbf{b})$, $S_y(\mathbf{b})$, $S_z(\mathbf{b})$, $S_\theta(\mathbf{b})$, $S_\phi(\mathbf{b})$, are required according to the spatial state of a cylinder defined by its state vector $\mathbf{b}$ (generalized coordinate vector), which is composed of a vector of translation $\mathbf{b}_t$ and a vector of rotation $\mathbf{b}_r$. We define the center of the focus as the origin of the Cartesian coordinate system. The angle between the optical and the cylinder axis is the polar angle b_θ. The azimuthal angle is b_ϕ. The rotation angle b_ψ about the cylinder axis cannot be detected because of its intrinsic symmetry. We define

$$\mathbf{b}=\left(\mathbf{b}_t,\;\mathbf{b}_r\right);\mathbf{b}_t=\left(b_x,b_y,b_z\right);\mathbf{b}_r=\left(b_\theta,b_\phi\right) \qquad (6)$$

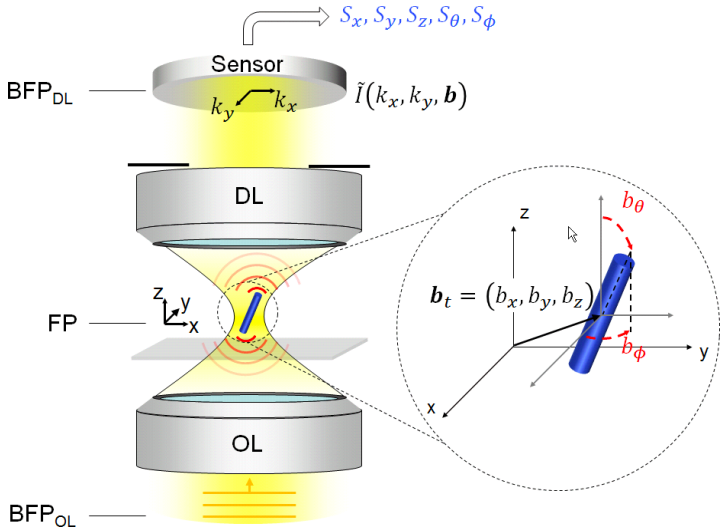

Fig. 1. Setup scheme for trapping and tracking. A cylinder is optically trapped in a laser focus and changes its center position and orientation due to external forces or thermal fluctuations. The interference intensity pattern of scattered and unscattered light is recorded by a sensor in the back focal plane (BFP) of the detection lens (DL). Zoom: a translated and tilted cylinder, described by a position vector $\mathbf{b}_t$ and an orientation vector $\mathbf{b}_r = (b_\theta, b_\phi)$.

3. Calculation of the electric field scattered at a cylindrical particle

3.1 Rayleigh-Gans Theory

A useful approach to calculate scattered fields at particles smaller or equal to the wavelength is the Rayleigh-Gans theory, also known as Born approximation. This approach assumes a single change of the k-vector of each incident plane wave (component), corresponding to the approximation that the field inside the particle does not change its angular spectrum, but only its amplitude. This amplitude is controlled by the polarizability α.

The Rayleigh-Gans theory requires that the maximum phase shift of the incident field induced by a particle of length L and of refractive index n_s relative to the surrounding medium with index n_m is small, i.e. $\Delta\Phi = L\, k_0(n_s\text{-}n_m) << 2\pi$. k_0 is the wave number in vacuum, and $k = n_m\, k_0$ the wave number in the medium. The polarizability in the scalar case according to the Clausius-Mossotti relation reads $\alpha = 3V(n_s^2\text{-}n_m^2)/(n_s^2 + 2n_m^2)$, where V is the volume of the particle. We start with the inhomogeneous Helmholtz equation for the electric field

$$\left(\Delta + k^2\right)\mathbf{E}(\mathbf{r}) = \hat{\boldsymbol{\alpha}}\, s(\mathbf{r})\, n_s{}^2 k_0{}^2 \mathbf{E}(\mathbf{r}) \qquad (7)$$

which is characterized by a shape function $s(\mathbf{r})$ describing the spatial extent of the scatterer with refractive index n_s such that $s(\mathbf{r}) = 1/V$ inside and $s(\mathbf{r}) = 0$ outside the scatterer. In general, however, the polarizability $\hat{\boldsymbol{\alpha}}$ is a tensor. To simplify the math in this study and to better illustrate the ideas of our strategy, we use the scalar approximation of the electric fields and the polarizability. The total scalar field $E(\mathbf{r})$ that solves Eq. (7) can be separated in an incident and a scattered field.

$$E(\mathbf{r}) = E_i(\mathbf{r}) + E_s(\mathbf{r}) \approx E_i(\mathbf{r}) + \alpha k^2 \iiint s(\mathbf{r}')E_i(\mathbf{r}')G(\mathbf{r}-\mathbf{r}')d^3r' \qquad (8)$$

Here, we have applied the Rayleigh-Gans approximation by replacing the total field $E(\mathbf{r})$ by the incident field $E_i(\mathbf{r})$ in the Fredholm-integral. Essentially, the scattered field is a superposition of spherical waves $G(\mathbf{r})$ driven with the local amplitude $E_i(\mathbf{r})$ at every position within the volume of the scatterer. The scalar Green's function $G(\mathbf{r})$ is a solution of the

homogenous Helmholtz equation. Using the convolution symbol (*), the approximated scattered field in the focal plane (FP) can be written as

$$E_s(\mathbf{r}) = \alpha k^2 \left(E_i(\mathbf{r}) s(\mathbf{r})\right) * G(\mathbf{r}) \tag{9}$$

For a particle displaced and reoriented by the vector **b**, the shape function depends on two vector variables $s(\mathbf{r},\mathbf{b})$.

3.2 Scatter spectra in the Fourier domain

Since our tracking scheme is based on BFP detection, we take the 3D Fourier transform of the scattered field $\tilde{E}_s(\mathbf{k},\mathbf{b})$, which reads

$$\tilde{E}_s(\mathbf{k},\mathbf{b}) = \tfrac{\alpha k^2}{(2\pi)^3} \tilde{G}(\mathbf{k}) \left(\tilde{E}_i(\mathbf{k}) * \tilde{s}(\mathbf{k},\mathbf{b})\right) \tag{10}$$

$\tilde{E}_s(\mathbf{k},\mathbf{b})$ simplifies in the case of an incident plane wave $\tilde{E}_i(\boldsymbol{k}) = (2\pi)^3 E_0 \delta(\mathbf{k}-\mathbf{k}_i)$ to

$$\tilde{E}_s(\mathbf{k},\mathbf{b}) = \alpha k^2 \tilde{G}(\mathbf{k}) E_0 \tilde{s}(\mathbf{k}-\mathbf{k}_i,\mathbf{b}) \tag{11}$$

The form factor $\tilde{s}(\mathbf{k},\mathbf{b})$ is the Fourier transform of the shape function, which is $s(\mathbf{r},\mathbf{b}) = 1/V$ inside the particle and $s(\mathbf{r},\mathbf{b}) = 0$ outside. For a non-tilted cylinder of length L, of diameter D and of volume $V = L\,(D/2)^2\pi$ it is:

$$\tilde{s}_0(\mathbf{k}) = \tfrac{2\,J_1(k_r D/2)}{k_r D/2} \operatorname{sinc}(k_z L/2) \tag{12}$$

where J_1 is the 1st order Bessel function and $\operatorname{sinc}(x) = \sin(x)/x$.

If the cylinder is translated by $\mathbf{b}_t$, $s(\mathbf{r}\text{-}\mathbf{b}_t)$, we find the form factor modulated, $\tilde{s}(\mathbf{k},\mathbf{b}_t) = \tilde{s}_0(\mathbf{k}) \exp(i\,\mathbf{k}\,\mathbf{b}_t)$. If in addition the cylinder is rotated by the angles $\mathbf{b}_r = (b_\theta, b_\phi)$, such that **k** is replaced by the Euler rotated vector $\mathbf{k'}(\mathbf{b}_r) = R_{y'}(b_\theta)\cdot R_z(b_\phi)\cdot\mathbf{k}$, the form factor for the general position state **b** can be expressed as

$$\tilde{s}(\mathbf{k},\mathbf{b}) = \mathrm{FT}\{s(\mathbf{r},\mathbf{b})\} = \tilde{s}_0\left[\mathbf{k}'(\mathbf{b}_r)\right] \exp(i\,\mathbf{k}\,\mathbf{b}_t) \tag{13}$$

It is advantageous that the operations for tilting and translating can be separated into two factors. The first term $\tilde{s}_0[\mathbf{k}'(\mathbf{b}_r)]$ describes the rotation of the scatterer by $\mathbf{b}_r$ and is real for symmetric scatterers such as cylinders. The second is a pure phase modulation and describes the scatterer's translation $\mathbf{b}_t$ from the center of the focus. The used rotation matrices are defined as

$$R_{y'}(\theta) = \begin{pmatrix} \cos(\theta) & 0 & \sin(\theta) \\ 0 & 1 & 0 \\ -\sin(\theta) & 0 & \cos(\theta) \end{pmatrix}; R_z(\phi) = \begin{pmatrix} \cos(\phi) & -\sin(\phi) & 0 \\ \sin(\phi) & \cos(\phi) & 0 \\ 0 & 0 & 1 \end{pmatrix} \tag{14}$$

The convolution term in Eq. (10) for an arbitrary incident wave reads

$$\tilde{E}_i(\mathbf{k}) * \tilde{s}(\mathbf{k},\mathbf{b}) = \iiint \tilde{E}_i(\mathbf{k}_i)\,\tilde{s}_0\left[\mathbf{k}'(\mathbf{b}_r) - \mathbf{k}_i\right] \exp\left(i(\mathbf{k}-\mathbf{k}_i)\mathbf{b}_t\right) d^3k_i \tag{15}$$

Therefore the scattered field in k-space for an incident plane wave is

$$\tilde{E}_s(\mathbf{k},\mathbf{b}) = \alpha k^2 E_0 \tilde{G}(\mathbf{k}) \tilde{s}_0\left[\mathbf{k}'(\mathbf{k},\,\mathbf{b}_r) - \boldsymbol{k}_i\right] e^{i(\mathbf{k}-\mathbf{k}_i)\mathbf{b}_t} \tag{16}$$

with $\tilde{G}(\mathbf{k})$ being the Fourier transform of G(**r**) as defined by Eq. (20). Assuming that the cylinder is a thin nanorod of length L and with diameter $D \ll \lambda$, it can be assumed to be a δ-like needle oriented in z-direction. Therefore the form factor is infinitely wide in lateral directions and only depends on the k_z component. The form factor of a very thin cylinder is

$$\tilde{s}_0(\mathbf{k}') = \sin c\left(k_z' L/2\right) \tag{17}$$

Now the Euler rotation of the cylinder is simplified massively, since $k'_z(b_\theta, b_\phi) = R_{y'}(b_\theta)\cdot R_z(b_\phi)\cdot \mathrm{k}\cdot \mathbf{e}_z$. Hence, we find for the rotated k_z -component:

$$k_z'(b_\theta, b_\phi) = \sin(b_\theta)\cos(b_\phi)k_x - \sin(b_\theta)\sin(b_\phi)k_y + \cos(b_\theta)k_z \tag{18}$$

with $k_z = (k^2 - k_x^2 - k_y^2)^{1/2}$. For a cylinder in the center of the focus and tilted only in the $k_x k_z$ plane ($b_\theta = 0$), the form factor reduces to

$$\tilde{s}_0(k_x, k_y, b_\theta) = \sin c\left(\left(-\sin(b_\theta)k_x + \cos(b_\theta)\sqrt{k^2 - k_x^2 - k_y^2}\right)L/2\right) \tag{19}$$

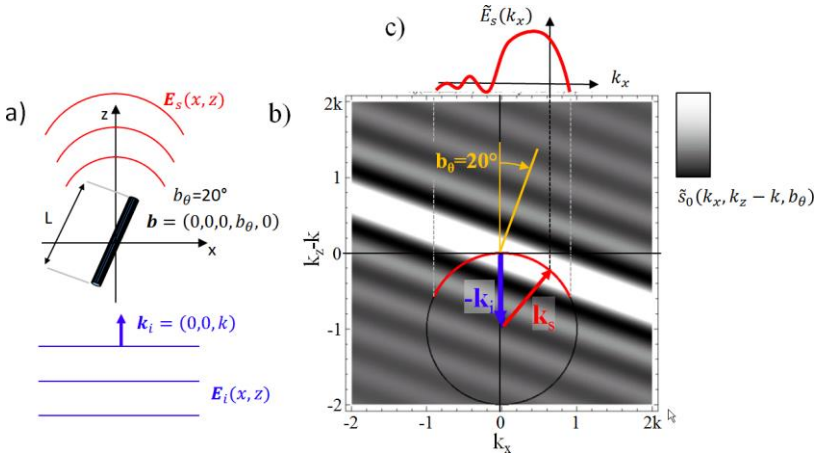

Fig. 2. Rayleigh-Gans scattering of infinitely thin cylinder of length L. a) A plane wave with wave-vector $\mathbf{k}_i$ incident on a tilted cylinder as local field approximation for the center of a focused field. b) The tilted form factor $\tilde{s}_0(k_x, k_z, b_\theta)$ of the cylinder (as background in grey scale) is shifted by $\mathbf{k}_i$ relative to the Ewald circle with radius $k_i = k_s$. The overlap (red circle area) defines the part of the angular spectrum of the forward scattered field $\tilde{E}_s(k_x)$ that is detected by a lens with $NA_{det} = 0.9$. c) The scattered field spectrum $\tilde{E}_s(k_x)$ as intersecting line between Ewald circle and form factor.

The Fourier transform of the Greens-function is the Ewald sphere, which is a spherical cap

$$\tilde{G}(\mathbf{k}) = \frac{1}{|\mathbf{k}|^2 - k^2} = \frac{1}{\left(k_x^2 + k_y^2 + k_z^2\right) - k^2} \tag{20}$$

The determination of the scattered field in k-space as described by Eq. (16) can be illustrated graphically as shown in Fig. 2. In a so-called Ewald construction, the spherical δ-like surface $\tilde{G}(\mathbf{k})$ is multiplied on the form factor $\tilde{s}_0[\mathbf{k}'(\mathbf{k}, \mathbf{b}_r) - \mathbf{k}_i]$, which is shifted by the k-vector of the incident wave $\mathbf{k}_i$. Figure 2(a) displays a thin cylinder of length $L \approx 2\lambda$ in the center of the focus tilted by $b_\theta = 20°$ and an incident plane wave with $\mathbf{k}_i = (0,0,k)$. Figure 2(b) shows the form factor in gray scale revealing the shape of a sinc-function also tilted by $b_\theta = 20°$ and shifted upwards by $\mathbf{k}_i$. The Ewald sphere is displayed as a black circle, whereas the part of the half circle representing the forward scattered field captured by the detection lens with $NA_{det} = 0.9$

is colored in red. The intersection is projected onto the k_x-axes and is displayed schematically as $\tilde{E}_s(k_x)$.

4. Interference of the incident and scattered angular field spectrum

In the following the angular spectrum representation of the fields $\tilde{E}(k_x,k_y)=\int_0^\infty \tilde{E}(\mathbf{k})dk_z$ propagating in positive z-direction is used, which is obtained by projecting the fields $\tilde{E}(\mathbf{k})$ located on the positive (negative) half of the Ewald sphere $\tilde{G}^+(\mathbf{k})$ with $k_z > 0$ ($\tilde{G}^-(\mathbf{k})$ with $k_z < 0$) onto the k_xk_y plane. This allows to use the more compact formulation:

$$\tilde{G}^{\pm}(\mathbf{k})\tilde{E}(\mathbf{k})=\tilde{E}\left(k_x,k_y,\pm k_z=\pm\sqrt{k^2-k_x^2-k_y^2}\right) \tag{21}$$

Hence, the angular spectrum of the scattered field for an incident plane wave (Eq. (16)) is

$$\tilde{E}_s\left(k_x,k_y,\mathbf{b}\right)=\tfrac{\alpha k^2}{(2\pi)^3}E_0\,\tilde{s}_0\left[\boldsymbol{k}'\left(k_x,k_y,\sqrt{k^2-k_x^2-k_y^2},\mathbf{b}_r\right)-\mathbf{k}_i\right]e^{-i(\mathbf{k}-\mathbf{k}_i)\mathbf{b}_t} \tag{22}$$

The interference intensity consists of three terms as denoted in Eq. (1). Since the incident intensity will be canceled out or subtracted as will be shown in the next section, the 5D position vector **b** has to be extracted from the remaining two terms.

In typical experimental situations the intensity of the incident field is removed electronically such that $|\tilde{E}_i|^2$ will be removed in the following. The relevant difference intensity reads:

$$\tilde{I}_{diff}(\mathbf{b})=\left|\tilde{E}_i+\tilde{E}_s(\mathbf{b})\right|^2-\left|\tilde{E}_i\right|^2=\left|\tilde{E}_s(\mathbf{b})\right|^2+2\left|\tilde{E}_i\right|\left|\tilde{E}_s(\mathbf{b})\right|\sin\left(\Delta\Phi_t(\mathbf{b})\right) \tag{23}$$

Here we used the fact that the phase of the scattered field Φ_s of a higher refracting particle in the Rayleigh-Gans-regime is $\pi/2$ behind the phase of the incident field Φ_i such that

$$\cos\left(\Delta\Phi(\mathbf{b})\right)=\cos\left(\Phi_i-\pi/2-\Phi_s(\mathbf{b})\right)=\sin\left(\Delta\Phi_t(\mathbf{b})\right) \tag{24}$$

The angular spectrum representation of a highly focused incident field without considering apodization is

$$\tilde{E}_i\left(k_x,k_y\right)=E_{i0}\,step\left(k_0NA-\sqrt{k_x^2+k_y^2}\right) \tag{25}$$

with the Heavyside step function defined by step(x) = 1 if $x \geq 0$ and step(x) = 0 otherwise. *NA* = $n_m\sin(\alpha_m)$ is the numerical aperture of the focusing lens. This corresponds to the field distribution in the pupil plane of an objective lens.

4.1 Calculation of the focused incident field

The only slightly more complicated part in describing Eq. (23) is the complex amplitude of the scattered field $E_s(\mathbf{b}_t)$ at the scatterer position $\mathbf{b}_t$, which is defined by the amplitude of the focused incident field. $E_i(\mathbf{b}_t)$ can be well described by a Fourier transform of the pupil plane:

$$\begin{aligned}E_i(\mathbf{r})&=\tfrac{1}{(2\pi)^3}\iiint\limits_{k_\perp<k_0NA}\tilde{E}_i(\mathbf{k})\cdot\exp\left(-i\mathbf{kr}\right)d^3k\\&=\tfrac{1}{(2\pi)^2}\iint\tilde{E}_i(k_x,k_y)\cdot e^{-i(k_xx+k_yy+k_zz)}/k_z\;dk_xdk_y\end{aligned} \tag{26}$$

with $k_z = (k^2\text{-}k_x^2\text{-}k_y^2)^{1/2}$. This method is very flexible since it allows to consider many relevant focusing aspects, but requires numerical computation. Alternatively, Gaussian beam optics can be used, which is a paraxial approximation, but is helpful in our context, where

interferometric tracking principles are to be developed. The field of a focused Gaussian beam can be written as

$$E_i(x,y,z) = \frac{A_0\, W_0}{W(z)} e^{-(x^2+y^2)/W(z)^2} e^{i\Phi_G(x,y,z)} \tag{27}$$

with a phase function considering the Gouy phase shift by totally $\Delta\Phi = \pi$ along the axial extent of the focus

$$\Phi_G(x,y,z) = \frac{k\left(x^2+y^2\right)}{2R(z)} + k\, z + \mathrm{a\,tan}\left(z / z_0\right) \overset{z<z_0}{\approx} + k\, z + \mathrm{a\,tan}\left(z / z_0\right) \tag{28}$$

Here, A_0 is the field strength, W_0 the beam waist at $z = 0$ and $W(z) = W_0[1 + (z/z_0)^2]^{1/2}$ for $z \neq 0$, $R(z) = z[1 + (z_0/z)^2]$ is the radius of curvature of the wave-front and $z_0 = k\, W_0^2/2$ is the Rayleigh length. The beam waist can be expressed by the NA of the lens such that $W_0 = 2^{1/2}\lambda/(\pi\, NA)$. From this it is possible to get a reasonable value for the complex amplitude $E_i(\mathbf{r} = \mathbf{b}_t) \approx |\, E_i(b_x, b_y, b_z)\,|\, exp[i\, atan(b_z / z_0) - i\, k\, b_z]$ at the center of the scatterer.

4.2 Local Field Approximation

Computing the scattered fields of a cylindrical particle in a highly focused laser beam is a complicated task. However, a particle, which is much smaller than the wavelength, is hardly affected by the spatial variation of the incident field across its extent. Therefore one can use the approximation of a local field with a mean phase at the center of the particle. In consequence, we assume that the particle "sees" an incident plane wave, which means that an incident plane wave is scattered according to Eq. (11). To account for the focused incident field we take the complex amplitude $E_i(\mathbf{r} = \mathbf{b}_t)$ of the focused beam. This approximation has turned out to provide scattering cross-sections for Rayleigh-Gans particles, which are not more than 20% away from the rigorously calculated scattered fields (Rohrbach – unpublished data).

Applying the local field approximation with $\mathbf{k}_i = (0,0,k)$, we can insert Eqs. (16) and (25) into Eq. (23) to obtain the interference part $\tilde{I}_{diff}(\mathbf{b})$ of the total intensity.

$$\begin{aligned} \tilde{I}_{diff}(\mathbf{k},\mathbf{b}) = \left|\tilde{E}_s(\mathbf{b})\right|^2 + 2\left|E_{i0}\, step\left(k_0 NA - \sqrt{k_x^2 + k_y^2}\right)\right| \cdot \\ \left|\frac{\alpha k^2}{(2\pi)^3}\, E_i(\mathbf{b}_t)\, \tilde{s}_0\left[\mathbf{k}'(\mathbf{k},\, \mathbf{b}_r) - \mathbf{k}_i\right]\right| \sin\left(\Delta\Phi_t(\mathbf{k},\mathbf{b}_t)\right) \end{aligned} \tag{29}$$

The interference phase $\Delta\Phi_t(\mathbf{k},\mathbf{b}_t)$ is determined by the phase of the scattered field translated by $\mathbf{b}_t$. Furthermore, we disregard the small changes of the lateral wavefront curvature in the local field approximation such that $\Phi_i(\mathbf{k},\mathbf{b}_t) = \Phi_i(k_z,b_z)$. We find [32]:

$$\begin{aligned} \Delta\Phi_t\left(k_x, k_y, \boldsymbol{b}_t\right) &= \left(\mathbf{k} - \mathbf{k}_i\right)\mathbf{b}_t + \Phi_i\left(\mathbf{k},\mathbf{b}_t\right) \\ &= \left[b_x k_x + b_y k_y + b_z k_z - b_z k\right] + \left[\mathrm{a\,tan}\left(b_z / z_0\right) + b_z k\right] \\ &= b_x k_x + b_y k_y + b_z\sqrt{k^2 - k_x^2 - k_y^2} + \mathrm{a\,tan}\left(b_z / z_0\right) \end{aligned} \tag{30}$$

Across the circular BFP of the detection lens, defined by $step(k_0 NA - (k_x^2 + k_y^2)^{1/2})$ the interference intensity reads:

$$\tilde{I}_{diff}^{O}(\mathbf{k},\mathbf{b}) = \left|\tilde{E}_s(\mathbf{b})\right|^2 + 2B\left|E_i(\mathbf{b}_t)\right| \left|\sin c\left(\left(k_z'(\mathbf{b}_t) - k\right)L/2\right)\right| \sin\left(\Delta\Phi_t(\mathbf{k},\mathbf{b}_t)\right) \tag{31}$$

with factor $B = E_{i0}\, \alpha k^2/(2\pi)^3$. The shape of the interference term in the BFP is determined by a sinc function for a cylinder tilt and by a sine function for a cylinder shift. These

characteristic intensity distributions can be illustrated by applying the thin cylinder approximation of Eq. (19) with b_ϕ = 0. For a cylinder in the beam center ($\mathbf{b}_t$ = 0) the interference term $\sin(\Delta\Phi_t(k_x,k_y,0))$ = 0 disappears and we find

$$\tilde{I}^O_{diff}\left(k_x,k_x,0,b_\theta\right)=B^2\left|\sin c\left(\left(-\sin\left(b_\theta\right)k_x+\cos\left(b_\theta\right)\sqrt{k^2-k_x^2-k_y^2}-k\right)L/2\right)\right|^2 \quad (32)$$

For tilt angles b_θ < 30° and in the paraxial approximation, where $k_z = k - k_x^2/2k - k_y^2/2k$ the interference intensity with b_ϕ = 0 results in

$$\tilde{I}^O_{diff}\left(k_x,k_x,0,b_\theta\right)=B^2\left|\sin c\left(\left(-b_\theta k_x-k_x^2/2k-k_y^2/2k\right)L/2\right)\right|^2 \quad (33)$$

This equation is illustrated in Figs. 3(a)-3(c) for a cylinder at $\mathbf{b}_t$ = 0 and for different tilt angles b_θ = 0, 10°, 20°. The $|\text{sinc}|^2$ function is shown as a bright circular region in the BFP and is shifted linearly with increasing tilt angle b_θ as displayed in Fig. 3(d). The principle holds also for $b_\phi \neq 0$ as shown in Figs. 3(e), 3(f), where b_ϕ can be read out by the polar angle of the intensity's center-of-mass.

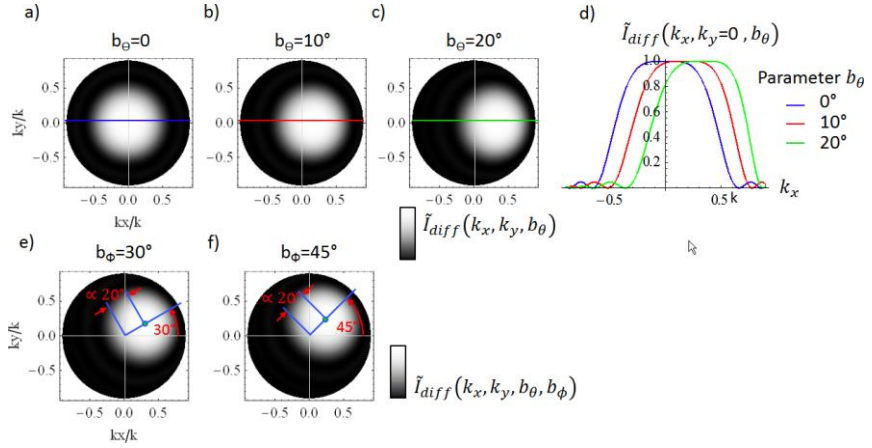

Fig. 3. Intensity difference $\tilde{I}^O_{diff}(k_x,k_y)$ in the BFP of the detection lens for a tilted cylinder. a-c) The flat-top like intensity maximum shifted sideward if the cylinder is tilted ($b_\theta > 0$, $b_\phi = 0$). d) Corresponding intensity line scans. e,f) For $b_\phi \neq 0$ the center of mass of $\tilde{I}^O_{diff}$ is shifted in direction of the tilt (b_θ, b_ϕ).

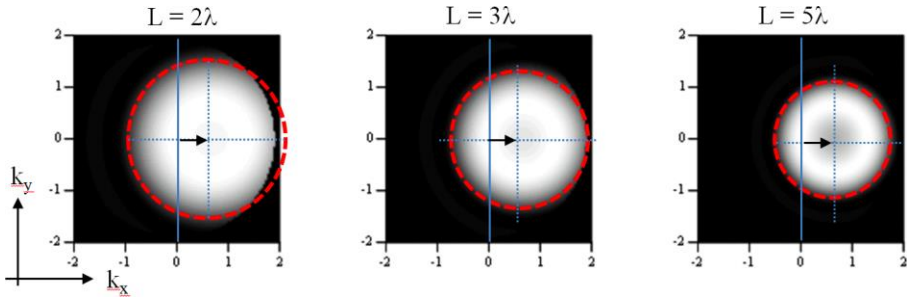

Fig. 4. Influence of a cylinders length on the intensity difference $\tilde{I}^O_{diff}(k_x,k_y)$. With increasing length L the width of the flat-top like intensity maximum (red circle) is decreased. The tilt angle b_θ is defined by the length of the circle's center vector (arrow).

The diameter of the $\text{sinc}[(-k_x^2-k_y^2)L/(4k)]$ function is determined by the length L of the cylinder, such that the bright area becomes narrower for longer cylinders (see Fig. 4).

Now, how does an additional shift $\mathbf{b}_t$ of the cylinder change the intensity distribution in the BFP? To illustrate the multiplication with the $\sin[\Delta\Phi_t(k_x,k_y,\mathbf{b}_t)]$ function as described in Eq. (29), we extend Eq. (33) for the case $\mathbf{b}_t = (b_x,0,0)$ such that

$$\tilde{I}^{O}_{diff}\left(k_x,k_y,b_x,b_\theta\right)=\left|\tilde{E}_s\left(\mathbf{b}\right)\right|^2+B\left|E_i\left(0\right)\right|\left|\sin c\left(\left(-b_\theta k_x-\frac{k_x^2+k_y^2}{2k}\right)L/2\right)\right|\sin\left(b_x k_x\right) \quad (34)$$

The combination of a cylinder shift and tilt is displayed in Fig. 5 with the interference intensities $\tilde{I}^{O}_{diff}(k_x,k_y,\mathbf{b}_t,b_\theta)$ shown in gray scale and three line scans each on the right side. The multiplication with either $\sin(b_x k_x)$ as shown in Figs. 5(a)-5(c) or with $\sin(b_y k_y)$ as in Fig. 5(d) reveals a modulation of the |sinc| function in the BFP, which is approximately linear with the cylinder displacement in the FP. Again, the tilt of the cylinder in the FP results in a shift of the circular region. This principle implies a 5D detection scheme, which is achieved by the method of a local quadrant photo-diode (QPD).

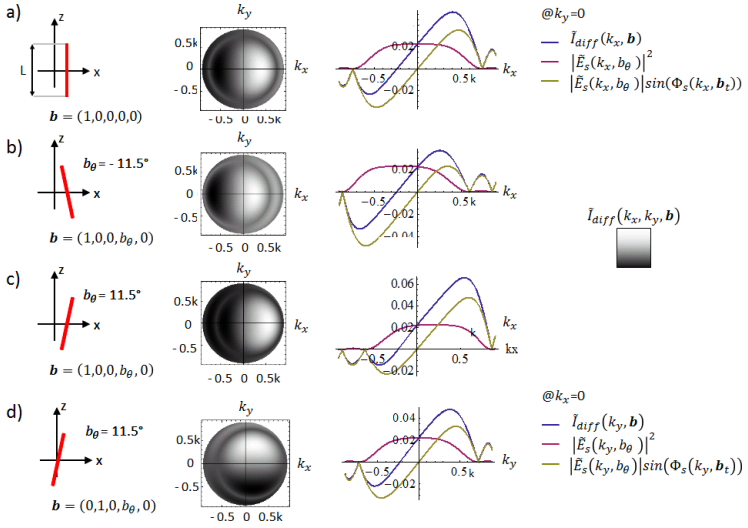

Fig. 5. Tracking signals for a thin cylinder, which is both shifted and tilted. Left column: Scheme for shifted and tilted cylinders. Center column: Corresponding intensity difference $\tilde{I}^{O}_{diff}(k_x,k_y)$ in the BFP. Right column: intensity line can $\tilde{I}^{O}_{diff}(k_x,0)$ illustrate the signal shift for a cylinder tilt and the bipolar signal modulation for a cylinder shift.

A displacement b_z of the cylinder in axial direction results in a spherical modulation of $\tilde{I}^{O}_{diff}(k_x,k_y,\boldsymbol{b}_t,b_\theta)$ with the axial phase $b_z(k^2-k_x^2-k_y^2)^{1/2}+\mathrm{a}\tan(b_z/z_0)$. The intensity modulation is ring like as illustrated by Fig. 6.

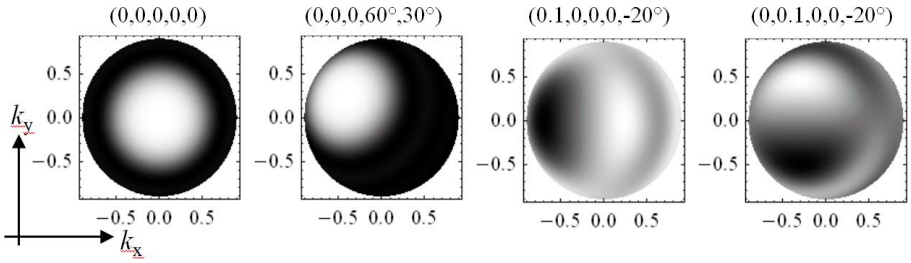

Fig. 6. Intensity difference $\tilde{I}^{O}_{diff}(k_x,k_y,\boldsymbol{b})$ for axially displaced thin cylinders with arbitrary positions and orientations, decribed by the state vector $\mathbf{b} = (\mathbf{b}_t, \mathbf{b}_r) = (b_x,b_y,b_z,b_\phi,b_\theta)$. A cylinder shift in axial direction results in a sphercial modulation of the signal.

4.3 Comparison with rigorous numerical approach

The analytical approach presented here contains a number of approximations, which were necessary to perform in order to derive a qualitative relationship between a cylinder tilt and shift and the interference intensity in the BFP. The qualitative correctness of the analytically approximated intensity $\tilde{I}^{O}_{\mathrm{diff}}(k_x, k_y, \mathbf{b})$ was therefore compared to rigorous numerical calculations using the in-house simulation software Lightwave(R). Herewith a highly focused incident field with NA = 1.2 [33] was scattered at a cylinder of finite thickness D within the Rayleigh-Gans theory [31]. The numerical results confirm our evaluated principle that a cylinder shift / tilt in the FP results in a signal modulation/shift in the BFP as illustrated in the following Fig. 7.

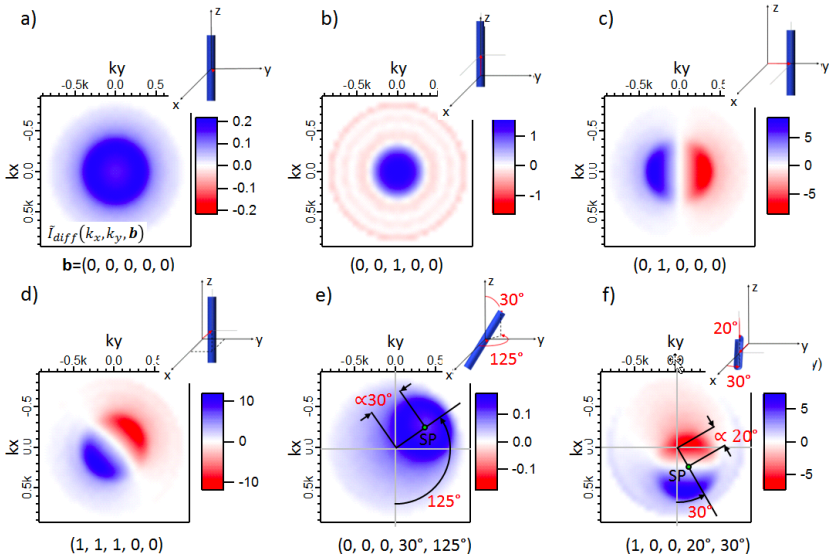

Fig. 7. Rigourously computed intensities $\tilde{I}^{O}_{diff}(k_x, k_y, \boldsymbol{b})$ for states $\mathbf{b} = (b_x, b_y, b_z, b_\theta, b_\phi)$ of a cylinder with finite thickness. The cylinder length is L = 0.8µm and the diameter is D = 0.1µm. The cylinders displacements are in units of 0.1µm. The round pattern $\tilde{I}^{O}_{diff}(k_x, k_y, \boldsymbol{b})$ is modulated in three cases and is shifted by the positions SP in e,f) to account for cylinder tilts.

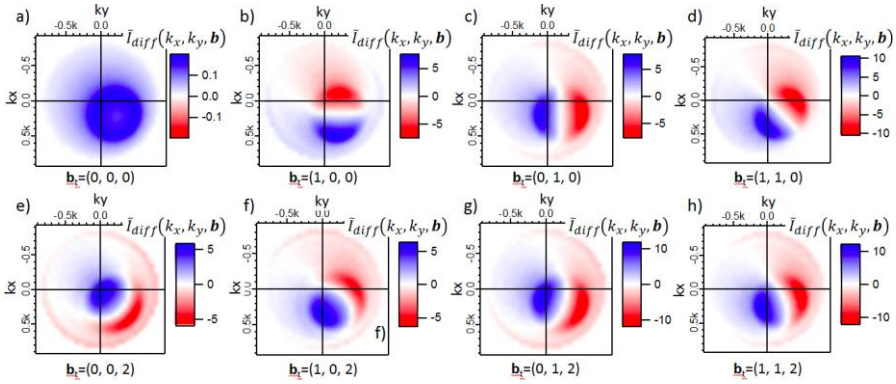

Fig. 8. Rigourously computed intensity differences $\tilde{I}^{O}_{diff}(k_x, k_y, \boldsymbol{b})$ for a tilted cylinder with positions $\mathbf{b} = (b_x, b_y, b_z, 20°, 45°)$. The cylinder length is L = 0.8µm, its diameter D = 0.1µm and its refractive index n_s = 1.57. The shifts are in units of 0.1µm. For a cylinder shift of b_z, the blue-red patterns within the area of the local QPD rotate from the top row (b_z = 0) to the bottom row (b_z = 0.2µm) due to a multiplication with $\sin(\Delta\Phi_t(k_x,k_y,b_z))$.

However, there are cases in which intensities $\tilde{I}^{O}_{\mathrm{diff}}(k_x,k_y,\mathbf{b})$ for different parameters look similar. Comparing for example, Figs. 8(d) and 8(f), one can see a slight clock-wise rotation of the bi-polar signal, which results from the spherical modulation of an axial cylinder shift. This effect, for instance, leads to an over-estimation of the cylinder shift along y.

5. Five-dimensional tracking with a local QPD

The goal of this study is to develop a tracking scheme, which allows to extract 5 signals S_x, S_y, S_z, S_θ, S_ϕ for position and orientation out of the BFP interference intensity in the back focal plane, which is $\tilde{I}^{O}_{diff}(k_x,k_y,b_x,b_y,b_z,b_\theta,b_\phi)$ + *const*. In addition, the desired scheme shall provide a roughly linear relationship between a cylinder state b_j and a signal $S_j \approx S_{0j} + g_{jj}\cdot b_j$, but also signals which are approximately independent of each other ($j = x,y,z,\theta,\phi$). The detector sensitivities g_{jj} define an diagonal matrix such that

$$\begin{pmatrix} S_x \\ S_y \\ S_z \\ S_\theta \\ S_\phi \end{pmatrix} \approx \begin{pmatrix} S_{0x} \\ S_{0y} \\ S_{0z} \\ S_{0\theta} \\ S_{0\phi} \end{pmatrix} + \begin{pmatrix} g_{xx} & & & & \\ & g_{yy} & & & \\ & & g_{zz} & & \\ & & & g_{\theta\theta} & \\ & & & & g_{\phi\phi} \end{pmatrix} \begin{pmatrix} b_x \\ b_y \\ b_z \\ b_\theta \\ b_\phi \end{pmatrix} \tag{35}$$

Based on the general BFP interference detection scheme introduced by Eq. (3), the spatial filter function $\mathbf{H}(k_x,k_y) = (H_x,H_y,H_z,H_\theta,H_\phi) = (\mathbf{H}_t(k_x,k_y),\mathbf{H}_r(k_x,k_y))$ must provide the 5 state variables b_j. As pointed out and illustrated in the last section, the tilt angles (b_θ,b_ϕ) can be extracted from the center of mass position $\mathbf{k}_c$ = (k_{xc},k_{yc}) of the circular intensity region of $\tilde{I}^{O}_{diff}(k_x,k_y)$. The radius of this circular region depends on the cylinder length and shall be denoted as k_L (see Fig. 9). This region can be described by a circular step function as $step\left(k_L - |\mathbf{k}-\mathbf{k}_c|\right)$.

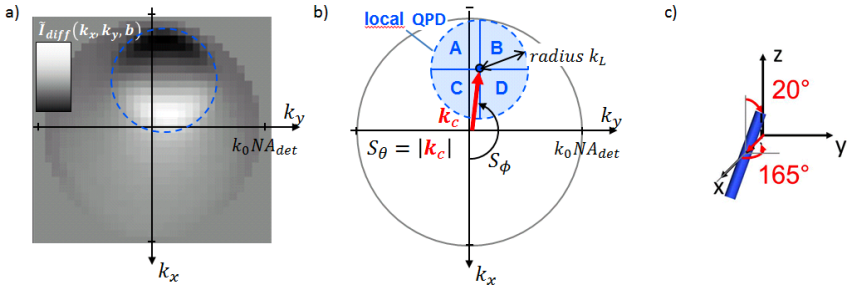

Fig. 9. Intensity read out with a local QPD. a) Computed intensity difference $\tilde{I}^{O}_{diff}(k_x,k_y,\boldsymbol{b})$ in the $\mathrm{BFP_{DL}}$ for a cylinder with state vector **b** in a focused laser beam. b) Scheme for a read out using a local QPD: A disc aperture with radius k_L, center position (k_{xc},k_{yc}) and distance $|\mathbf{k}_c|$, and the local QPD quadrants A, B, C and D. c) Corresponding shift and tilt of the cylinder.

The center of mass vector (k_{xc},k_{yc}) is determined from the interference part $\tilde{I}^{O}_{diff}$, which is evaluated above an intensity threshold defined by the 1/e fraction of the intensity maximum $\tilde{I}^{max}_{diff}$. The intensity above the threshold is defined as

$$\tilde{I}^{thr}_{diff}(k_x,k_y,\mathbf{b}) = \begin{cases} \left|\tilde{I}_{diff}(k_x,k_y,\mathbf{b})\right|, & \text{if } \left|\tilde{I}_{diff}\right| \geq \frac{1}{e}\tilde{I}^{max}_{diff} \\ 0, & \text{otherwise} \end{cases} \tag{36}$$

From this the center of mass vector $\mathbf{k}_c = (k_{xc},k_{yc})$ is obtained by the operation:

$$\mathbf{k}_c = \left(k_{xc},k_{yc}\right) = \frac{\iint \tilde{I}_{diff}^{thr}\left(k_x k_y,\mathbf{b}\right)\left(k_x,k_y\right)\,dk_x dk_y}{\iint \tilde{I}_{diff}^{thr}\left(k_x k_y,\mathbf{b}\right)\,dk_x dk_y} \tag{37}$$

Having determined $\mathbf{k}_c$, the concept of a local QPD can be applied, which evaluates the bipolar signal modulation within the circular region. In other words, the difference of the upper and lower half of the integrated detector area $step(k_L - |\mathbf{k}-\mathbf{k}_c|)(2step(k_y - k_{yc})-1)$ describes the vertical cylinder displacement and the difference of the left and right half, $step(k_L - |\mathbf{k}-\mathbf{k}_c|)(2step(k_y - k_{yc})-1)$ describes the horizontal cylinder displacement. The first three (translational) components of the 5D filter function read:

$$\mathbf{H}_t\left(k_x,k_y,\mathbf{k}_c\right) = step\left(k_L - |\mathbf{k}-\mathbf{k}_c|\right)\cdot\begin{pmatrix} 2\,step\left(k_x - k_{xc}\right)-1 \\ 2\,step\left(k_x - k_{xc}\right)-1 \\ 1 \end{pmatrix} \tag{38}$$

The last two (rotational) components of the 5D filter function are:

$$\mathbf{H}_r\left(k_x,k_y,\mathbf{k}_c\right) = \begin{pmatrix} \sqrt{k_{xc}^2 + k_{yc}^2} \\ \mathrm{a\,tan}(k_{xc}/k_{yc}) \end{pmatrix} \tag{39}$$

After having found the 5D spatial filter function $\mathbf{H}(k_x,k_y)$, we can express the relation between the 5D state of the nanorod and the corresponding tracking signal as an extension to Eq. (3):

$$S_j\left(b_j\right) = \iint \tilde{I}_{diff}^{thr}\left(k_x k_y,\boldsymbol{b}\right) H_j\left(k_x,k_y,\mathbf{k}_c\right) dk_x dk_y \approx S_{0j} + g_{jj}\times b_j \tag{40}$$

which is e.g. for displacements in direction b_x:

$$S_x\left(b_x,b_\theta\right) \approx B\left|E_i\left(0\right)\right|\cdot \iint \left|\sin c\left(\left(-b_\theta k_x - \left(k_x^2+k_y^2\right)/2k\right)\frac{L}{2}\right)\sin\left(b_x k_x\right)\left(2step\left(k_x - k_{xc}\right)-1\right)\right| dk_x dk_y \tag{41}$$

6. Tracking results

The five dimensional configuration space contains many different combinations of cylinder positions and tilts as well as corresponding interference patterns, which could be analysed. However, to illustrate that the classical Fourier relation of shift / tilt in the FP results in a modulation / shift in the BFP holds, only some typical cylinder states are shown here.

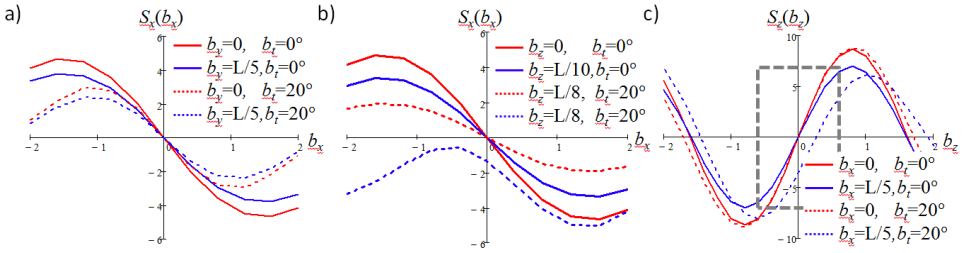

Fig. 10. Tracking signals $S_i(\mathbf{b})$ for a nanorod with different state vectors b. a) Lateral signals $S_x(b_x)$ for two different lateral shifts b_y and tilts b_θ. b) Lateral signals $S_x(b_x)$ for two different axial shifts b_z and tilts b_θ. c) Axial signals $S_z(b_z)$ for two different lateral shifts b_x and tilts b_θ. The linear detection range is marked with a box.

For a cylindrical nanorod optically trapped in a highly focused beam typical displacements are not larger than the extent of the focus and polar tilt angles are smaller than

b_θ = 30° due to restoring forces or torques that increase linearly with the displacement $\mathbf{b}_t$ or tilt angle b_θ respectively. The limits in $\mathbf{b}_t$ and $\mathbf{b}_r$ correspond roughly to the range of displacements where the linear relation of signals $S_j \approx S_{0j} + g_{jj} \cdot b_j$ can be assumed, as it is also known from the BFP tracking of spheres. Figure 10 displays the typical sinus-like shaped signals for rod displacements. Although the slopes vary slightly, the linear dependency for rod displacements smaller than 0.2 µm can be seen.

6.1 The iso-signal grid representation

In the following, the results from numerical simulations are presented, which have been computed on a grid with translations b_x = –0.2…0.2, b_y = –0.2…0.2, b_z = –0.2…0.6, in µm, with increment 0.1µm and tilt angles b_θ = 0…30°, with increment 10°, b_ϕ = 0…30°, with increment 15°, which yields 5 x 5 x 9 x 4 x 7 = 6300 different states of a cylinder. Two dimensional contour plots $S_i(b_i,b_j)$ and $S_j(b_i,b_j)$ (i,j = x,y,z,θ,ϕ) are overlaid to illustrate that most of the signals are approximately linear and pairwise orthogonal to each other, such that $S_i(b_i,b_j) = g_{ii}b_i$ and $S_j(b_i,b_j) = g_{jj}b_j$. Linearity is demonstrated by an equidistant spacing of the grid lines, orthogonality is shown by an orthogonal intersection of vertical and horizontal lines of equal signals (iso-lines), which are plotted in different colors for i and j in Fig. 11. Here, the simplest case is shown, for a non-tilted cylinder shifted over a range of 0.4µm × 0.8µm (Fig. 11(a)) and a centered cylinder, which is rotated over a range of 90° × 30° (Fig. 11(b)).

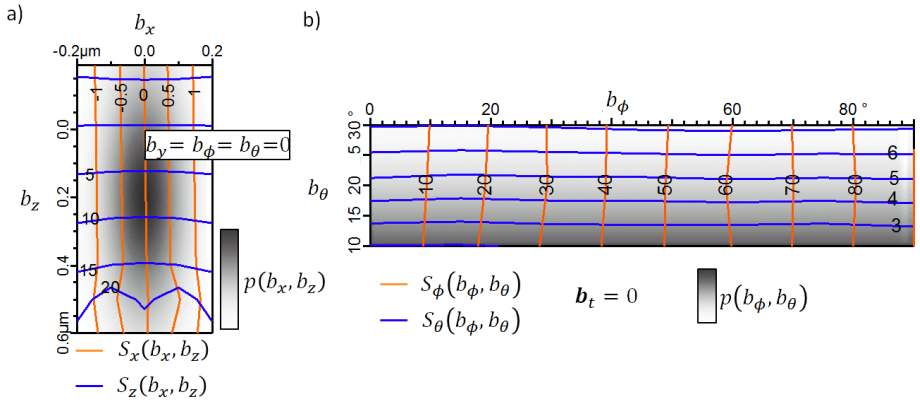

Fig. 11. Position and orientation signals of a cylinder in a focused laser beam. An assumed probability density of states is underlayed in the background in gray scale. a) Iso-lines $S_x(b_x,b_y)$ and $S_z(b_x,b_y)$ of a vertical cylinder centered in y-direction. b) Iso-lines $S_\phi(b_\phi, b_\theta)$ and $S_\theta(b_\phi, b_\theta)$ of a tilted cylinder in the center of the focus. The smallest polar angle is b_θ = 10°, since azimuth angles b_ϕ are not defined for b_θ = 0.

The gray shaded areas in the background of the contour plots indicate the probability densities $p(b_i,b_j)$ to find the nanorod in the corresponding states (positions or orientations) assuming a harmonic potential $W(b_i,b_j) \approx ½\cdot\kappa_i\cdot b_i^2 + ½\cdot\kappa_j\cdot b_j^2$ or a linear restoring force $\mathbf{F}_j(b_i) = -\partial/\partial b_j \; W(b_i)$, respectively. The probability densities $p(b_i,b_j)$ are defined according to Boltzmann statistics as

$$p(b_i,b_j) = p_{0ij}\, exp\left[-W(b_i,b_j)/(k_B T)\right] \approx \frac{1}{2\pi\sigma_i\sigma_j} exp\left[-\tfrac{1}{2}(b_i/\sigma_i)^2 - \tfrac{1}{2}(b_j/\sigma_j)\right] \quad (42)$$

Where p_{0ij} normalizes the probability distribution to 1. $\sigma_j = k_B T/\kappa_j$ is the standard deviation of the Gaussian distribution in direction b_j (j = x,y,z,θ) and results from the equipartition theorem (with $k_B T$ as the thermal energy). The coupling of translation and rotation is not considered. The probability distributions of the coordinates is assumed to be mutually independent such that $p(b_i,b_j) = p(b_i)p(b_j)$. The probability distribution for the orientation

azimuth angle b_ϕ is $p(b_\phi) = p_{0\phi} = 1/(2\pi)$ since no force or torque restores the nanorod along b_ϕ if polarization effects are disregarded. The overlays of the signals $S_{x/z}(b_\theta,b_{x/z})$ and $S_\theta(b_\theta,b_{x/z})$ in Fig. 12 as well as the signals $S_{x/z}(b_\phi,b_{x/z})$ and $S_\phi(b_\phi,b_{x/z})$ in Fig. 13 reveal that only weak signal coupling occurs according to our computer simulations. However, for axial displacements b_z = 0.2µm the signal iso-lines $S_x(b_{\theta/\phi},b_x)$ in Fig. 12(b) and Fig. 13(b) are rather oblique.

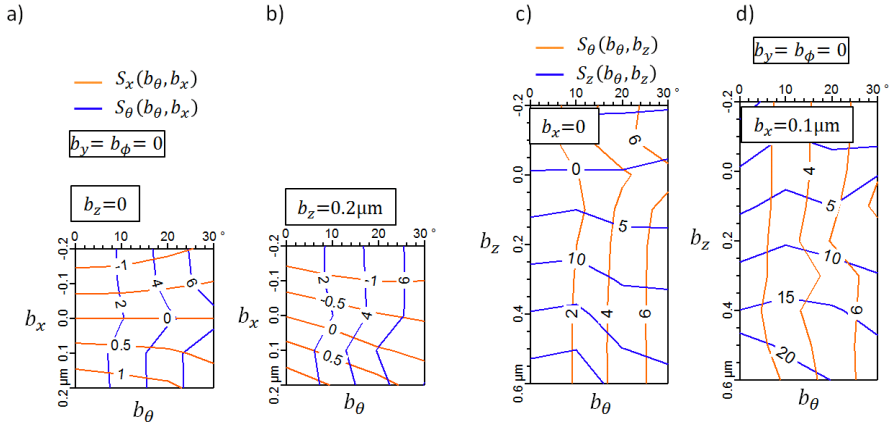

Fig. 12. Linearity and orthogonality of position and orientation signals $S_{x/z}(b_\theta,b_{x/z})$ and $S_\theta(b_\theta,b_{x/z})$ of a shifted and tilted cylinder in a focused laser beam. a), b) Iso-signal lines (in a.u.) with and without axial cylinder shift. c),d) Iso-signal lines (in a.u.) with and without lateral shift.

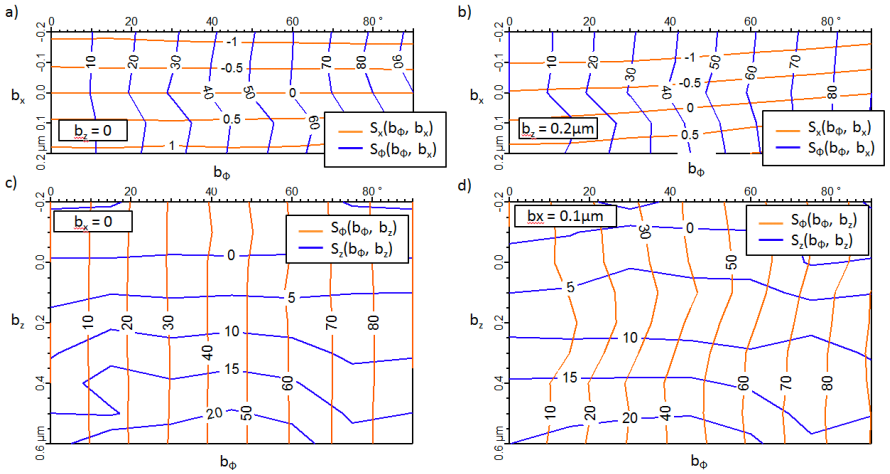

Fig. 13. Linearity and orthogonality of position and orientation signals $S_{x/z}(b_\phi,b_{x/z})$ and $S_\phi(b_\phi,b_{x/z})$ of a shifted and tilted cylinder in a focused laser beam. a), b) Iso-signal lines (in a.u.) with and without axial shift. c),d) Iso-signal lines (in a.u.) with and without lateral shift.

The signals for axial displacements and a polar angle tilt do couple as shown in Fig. 14, where both iso-signal lines are tilted by roughly the polar tilt angle for the cylinder. In this case the sensitivity matrix of Eq. (35) is not diagonal and the signals for a change in b_i can be expressed as

$$S_i\left(b_i,b_j\right) = g_{ii}\left(b_i\right)b_i + g_{ij}\left(b_j\right)b_j \approx g_{ii}b_i + g_{ij}b_j \qquad (43)$$

For increasing changes in b_i the sensitivities $g_{ii}(b_i)$ become space variant. In general all states of the cylinder couple with each other depending on the strength of b_i such that $S_i(\mathbf{b}) = g_{ii}b_i + \sum_{i \neq j} g_{ij}b_j + S_{0i}$.

The coupling between tilt and axial shift can be understood by inspecting Figs. 8(b) and 8(f), where the modulations of interference intensities are not independent in x,y and z.

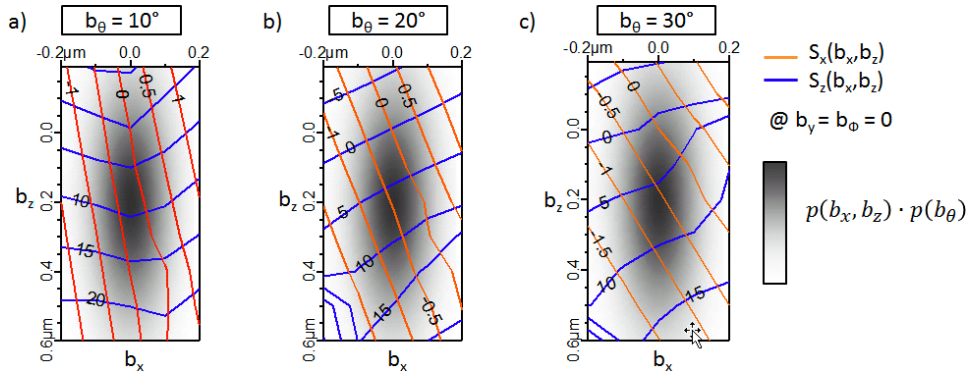

Fig. 14. Coupling of linear position and orientation signals $S_x(b_x,b_z)$ and $S_z(b_x,b_z)$ of a shifted and tilted cylinder in a focused laser beam. An assumed Gaussian probability density of states as a result of linear restoring forces is underlayed in the background in gray scale.

7. Calibration of the tracking system and error estimate

The standard technique to obtain the trap stiffnesses κ_{jj} and the detector sensitivities g_{jj} is to use the Langevin calibration method [27] for a particle diffusing in a harmonic potential. Here, the κ_{jj} can be measured via an autocorrelation function AC[$b_j(t)$], which decays exponentially in a harmonic potential $W(b_i)$ with autocorrelation time $\tau_{jj} = \gamma/\kappa_{jj}$. One can solve for κ_{jj} by using the translational drag coefficients $\gamma_\perp = 4\pi\ \eta\ L/(log(L/D) + \delta_\perp)$ and $\gamma_\parallel = 2\pi\ \eta\ L/(log(L/D) + \delta_\parallel)$ or, respectively, the rotational drag coefficient $\gamma_{rot} = \pi\ \eta\ L^3/(3log(L/D) + 3\delta_{rot})$ which is known from the dimensions D and L of the cylinder. Here η is the fluid's viscosity and δ are factors [34].

The detector sensitivities $g_{jj} = \sigma_{sj}/\sigma_j$ can be obtained from the standard deviations of the position or angle probability density, which is $\sigma_j = k_B T/\kappa_j$ according to the equipartition theorem, and the width σ_{sj} of the measured signal histograms. The histogram is generated from the trajectories $S_j(t) = S_j(b_j(t))$, which are measured for a couple of seconds. Since the g_{jj} are never constant across the diffusion volume, the widths σ_{sj} and the sensitivities g_{jj} represent mean values.

Therefore the reconstructed nanorod state b_j^{rec} is obtained $b_j^{rec} \approx S_j\ \sigma_j/\sigma_{sj}$. This results in a relative tracking error Δb_j, which is

$$\Delta b_j \approx S_j(\sigma_j / \sigma_{sj}) - b_j \qquad (44)$$

In our computer simulation we assumed realistic values for $\sigma_j = k_B T/\kappa_j$ as shown by the background gray colors in Fig. (14) From this we obtained the corresponding widths σ_{sj} and thereby $g_{jj} = \sigma_{sj}/\sigma_j$. Since we know the real input value b_j in the simulation, the error $\Delta b_j \approx b_j^{rec} - b_j$ can be estimated. This is shown for some typical states of a nanorod in Fig. 15.

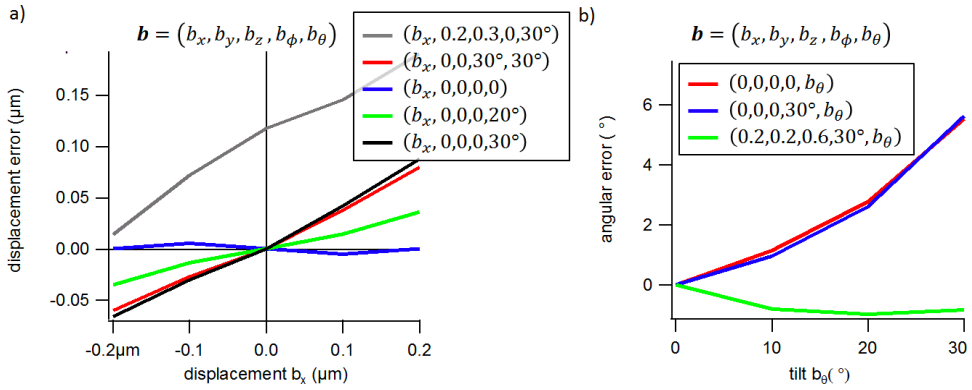

Fig. 15. Tracking errors for disaplcements and tilts of a cylinder (L = 0.8, D = 1µm, n_s = 1.57) a) Absolute tracking error for lateral displacements b_x for different state vectors **b**. b) Absolute tracking error for tilt angles $b_\theta$for different state vectors **b**. Results were calculated with the simulation software LightWave(R).

8. Discussion and conclusion

We have presented a theoretical concept of how to recover the 5-dimensional state $\mathbf{b} = (\mathbf{b}_t,\mathbf{b}_r)$ of a cylindrical nanorod (3D position $\mathbf{b}_t$ and two angles $\mathbf{b}_r$) from the interference pattern of unscattered light and light scattered at the cylinder. In particular, we present for the first time that the orientation tracking of a nanorod in a focused laser beam is also possible with the established concept of BFP-interferometry. Several difficulties had to be overcome, which might be one of the reasons why no such tracking concept has been presented yet.

Although rigorous scattering computations for a tilted cylinder in a highly focused laser beam have been published [20, 31], corresponding to a solution of the forward problem, the back ward problem, the recovery of both the 3-D position and the 2-D orientation could not be solved. More precisely, the required direct relation between a nanorod displacement or tilt in the FP and the corresponding change of the interference pattern in the BFP has not been revealed. To uncover this relation, we have developed an analytical model based on the Rayleigh-Gans scattering theory. Since the interference patterns have to be evaluated in the BFP of the detection lens, the electric fields are derived in k-space or in the angular spectrum representation, respectively. The analytical representation of the form factor for a tilted cylinder was simplified by the approximation that the cylinder of finite length is infinitely thin. In addition, we used a local field approximation, i.e. an incident plane wave to calculate the scattered field spectrum, since the lateral phase of the incident field does not change much for typical displacement of an optically trapped nanorod. This operation results in a shift of the form factor by the incident k-vector. The local change of the phase and amplitude of the incident focused field along z was computed by Gaussian beam optics including the Gouy-phase shift.

The interference pattern in the BFP was then obtained by the spectrum of a highly focused incident beam and by the approximated spectrum of the scattered field. From the analytical formula for the interference intensity and the corresponding 1D and 2D plots, it turned out that a nanorod displacement results in the modulation of the BFP interference intensity, whereas a tilt of the nanorod results in a shift of the BFP intensity. The results of our model with above mentioned approximations were confirmed by a rigorous numerical approach for a dielectric cylinder with L = 0.8µm = λ/n and D = 0.1µm, which were obtained by the in-house developed simulation software LightWave(R).

Over a reasonably wide range of displacements $\mathbf{b}_t$ and/or tilts $\mathbf{b}_r$ the 5 resulting signals $\mathbf{S}(\mathbf{b}) \approx \mathbf{S}_0 + \hat{\mathbf{g}}\cdot\mathbf{b}$ are roughly linear with **b** and roughly orthogonal to each other. Only for larger nanorod displacements and angles, the signals become more nonlinear and begin to couple. This is especially pronounced for a tilted cylinder displaced in the axial z-direction.

However, there are a number of means of how to reduce the inter-signal coupling and to increase the linear tracking range. Similar to the approaches that have been applied successfully for the tracking of spheres [30, 35], a spatial filter (function) in the BFP of the detection lens might help to improve the 5D tracking of small cylinders in the focal region of a highly focused beam.

Nanorods can align horizontally, i.e. parallel to the strongest component of the electric field inside the focus due to a polarization induced torque [36, 37]. By inspecting Fig. 2 similar scattered fields and interference patterns can be expected for a horizontally tilted and shifted cylinder, provided that the cylinder is shorter than the focal diameter, i.e. $L < \lambda/n_m$. However, further investigations are necessary to test whether in this case the resulting tracking signals are unique, linear and orthogonal.

The experimental realization of our theoretical concept remains open and is challenging, if a fast tracking rate of about 100 kHz is the goal. It appears to be difficult to record the intensity pattern by simply two QPDs, delivering eight signals in total. A straightforward approach seems to be the usage of fast cameras with a small number of pixels, which are on the market, also for the popular 1064nm trapping wavelength requiring InGaAs as sensor material. It remains to be shown, whether the here presented tracking concept can be verified under experimental conditions.

Nevertheless, the fast 5D tracking of cylindrical nanorods will enable a manifold of applications reaching from non-equilibrium local probe measurements to surface scanning with optically trapped, needle-like probes similar to AFM imaging. Furthermore, if nanorods are used as building blocks for nano-scaled systems, the observation of their thermal state fluctuations is indispensable for a controlled assembly.